Hybrid-Three-Level Current-Fed Series-Resonant Isolated DC-DC Converter and its Optimization Modulation Strategy

Fengjiang Wu, *Senior Member, IEEE*, Kaixuan Wang, and Suhua Luo

***Abstract*—In this article, a hybrid three-level current-fed series-resonant isolated bidirectional dc–dc converter is proposed, containing an interleaved parallel bidirectional buck/boost converter at the low-voltage side and a half-bridge three-level converter at the high-voltage side. The operation principles and characteristics of the proposed converter are thoroughly analyzed with the duty-cycle plus dual phase-shift control. The relationship between the general case of three independent control variables and the transfer power is derived. Then, a modulation strategy optimization algorithm by taking the minimum root mean square (rms) value of the resonant current as the objective function is presented. Under the optimal operation point, the converter operates efficiently with the minimum rms value of the resonant current and accordingly increases the efficiency. The detailed experimental results verify the correctness and feasibility of the proposed converter and modulation strategy.**

***Index Terms*—Bidirectional current-fed dc–dc converter, minimum resonant current, series-resonant, three-level.**

I. Introduction

THE isolated bidirectional dc–dc converter (IBDC) has a wide potential application prospects in the field of electric vehicles, renewable energy power generation and energy storage systems due to the unique advantages, such as soft-switching characteristic, high-frequency galvanic isolation, bidirectional power flow, etc. [1], [2].

The first popular type of topology of the IBDC is the voltage-fed dual active bridge (VF-DAB) converter. This topology is capable of a wide range of voltage bidirectional conversion. According to the type of the energy storage component, its topology mainly includes the inductor-type and resonant-type ones. The current stress of the inductor-type is at least twice the effective output current, resulting a poor current rating utilization and high system loss, which is not conductive to high power factor operation [3]–[6]. For the resonant converters, e.g., *LC*-type, *LLC*-type, *CLLC*-type, and so on, were reported in the literature. Among them, the *LC*-type converter has a simple structure and is easy to control. The shape of the transformer currents of the resonant-type one is close to the sinusoidal and the peak value of the transformer current is accordingly reduced to 1.414 of its rms value. Hence, the series resonant converter has a better electromagnetic characteristic and the current stress is reduced by 20% as compared to the inductor-type ones. The resonant capacitor can effectively filter out the dc component of the transformer and reduce the eddy current loss of the transformer winding [7]–[10]. Therefore, the resonant converter has attracted more and more attentions. However, when it is applied to a system with a wide voltage variation range, the normalized voltage amplitude on both sides of the transformer is usually not matched, causing the ratio of the peak value/root mean square (rms) value of the resonant current to be too large in the entire power range, which reduces the utilization rate of the system hardware rated capacity [11], [12]. In addition, the VF-DAB converter has high input current ripple, which reduces the life time of the power sources. The additional filter devices increase the system volume and cost.

Another type of topology is the current-fed dual active bridge (CF-DAB) converter. According to the current source structure, CF-DAB converter can be divided into two classes, i.e., the series inductor-type and the interleaved parallel-type (or L-L type), where the series inductor-type converter has the smallest current stress. However, it can realize only the boost conversion in one power flow direction, because the series inductor-type converter is essentially equivalent to a boost dc–dc converter. In addition, the voltage spike induced by the transformer leakage inductor is serious, when two inductor currents are not matched during the transition of circuit state. It is necessary to add an active clamp circuit or improve the modulation strategy, which results an increase in the manufacturing and control cost [13], [14].

The interleaved parallel CF-DAB converter has two parallel inductors on the input side. The converter can be equivalent to an interleaved parallel buck/boost dc–dc converter and a VF-DAB converter. Therefore, no additional auxiliary snubber circuit is required and the input current ripple can be reduced by the interleaved technology. In addition, when the input voltage varies in a wide range, the added dc capacitor can ensure that the equivalent VF-DAB converter always operates with the optimal normalized voltage gain and achieves the optimal current characteristics,

Manuscript received January 9, 2021; revised March 28, 2021 and June 6, 2021; accepted July 15, 2021. Date of publication July 21, 2021; date of current version September 16, 2021. This work was supported in part by the National Natural Science Foundation of China under Grant 51877050. Recommended for publication by Associate Editor M. Ordonez. *(Corresponding author: Suhua Luo.)*

Fengjiang Wu and Kaixuan Wang are with the Department of Electrical Engineering, Harbin Institute of Technology, Harbin 150001, China (e-mail: shimeng@hit.edu.cn; 19b906021@stu.hit.edu.cn).

Suhua Luo is with the Department of Physics, Harbin Institute of Technology, Harbin 150001, China (e-mail: shual@hit.edu.cn).

Color versions of one or more figures in this article are available at https://doi.org/10.1109/TPEL.2021.3098452.

Digital Object Identifier 10.1109/TPEL.2021.3098452

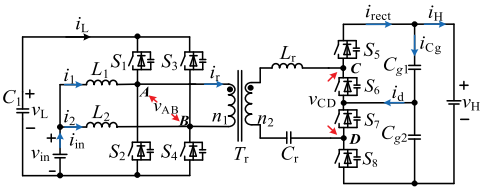

Fig. 1. Schematic of the proposed converter.

which is beneficial to improve the converter efficiency [15]–[20]. The operation principle of this type converter is analyzed in detail in [23] and it proved that it can realize the bidirectional buck-boost conversion.

Considering that the interleaved parallel CF-DAB converter possesses the advantages mentioned above and in order to extend its application field, in this article, a hybrid-three-level interleaved parallel resonant-type CF-DAB converter is proposed, where a half-bridge three-level structure is assigned on the high voltage side (HVS). Furthermore, an optimized modulation strategy to minimize the rms value of the resonant current is proposed based on pulsewidth modulation (PWM) plus dual-phase-shift (DPS) modulation. The proposed converter and its modulation have the following features. The input current is continuous and the ripple is greatly reduced. The voltage stress on the HVS switches is only half of the HVS bus voltage. When it is used in a low-voltage system, the power loss can be reduced because the on-state resistance of the power switches with a low rated voltage is usually low [24]–[26]. Considering that the rated voltage of existing mass-produced high-frequency power switches, such as SiC MOSFETs are still low, the three-level structure provides an approach that the SiC-based power switches are used in the higher voltage systems. Furthermore, the interleaved parallel structure combined with the proposed modulation strategy can eliminate internal reactive power of the equivalent resonant converter and achieve minimum rms value of the resonant current in the entire operating range, thus ensuring the high efficiency operation of the converter.

II. Proposed Converter and Operation Principles

A. Proposed Converter

The proposed hybrid-three-level current-fed series-resonant IBDC is shown in Fig. 1. The input dc inductors L_1, L_2 with the same inductance, the dc link capacitor C_1 and S_1-S_4 on the low voltage side (LVS) compose the interleaved parallel buck/boost converter. S_1-S_4 also compose an H-bridge converter. S_5-S_8 and the voltage spilt capacitors C_{g1}, C_{g2} on the HVS compose the half-bridge three-level converter. L_r and C_r compose a resonant tank as an intermediate energy storage link to transfer power between LVS and HVS. C_r is also used as a part of the three-level converter, which filters out the dc component of the transformer and prevent the transformer core from being saturated. The average voltage across C_r is half of the voltage on the HVS (v_H). The LVS and HVS are linked by a high-frequency transformer (HFT) T_r with the winding turns ration of n_1:n_2, which achieves the electrical isolation and voltage matching.

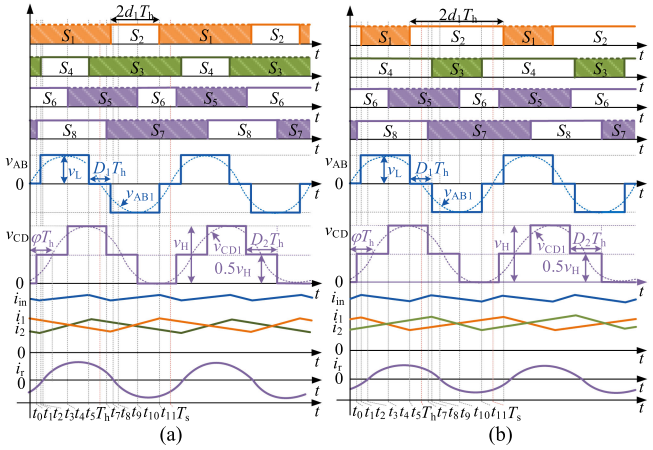

Fig. 2. Key waveforms of the PWM plus DPS modulation. (a) Mode I: d_1 <0.5. (b) Mode II: $d_1 > 0.5$.

The H-bridge converter on the LVS, the *LC* resonant tank, the HFT and the three-level converter on the HVS compose an equivalent *LC* resonant converter. The interleaved parallel converter on the LVS provides one more controllable degree of freedom, namely the voltage of C_1 (v_L), which is the input voltage of the H-bridge converter on the LVS. Therefore, v_L can always match v_H by regulating the duty cycle of the H-bridge converter on the LVS, to ensure the equivalent resonant converter always operates at its optimal current point, thus improve the converter efficiency and reduce the current stress.

B. Operation Principle

The proposed converter provides bidirectional power flow. When the power flows from the LVS to the HVS, the converter operates under the forward mode, otherwise, it operates under the backward mode. The operation principle of the two modes is exactly the same, so in this article only the forward mode is analyzed in detail. Ignoring the effect of the dead time, under the fixed-frequency PWM plus DPS modulation, the key operation waveforms in the forward mode are shown in Fig. 2. The current of the two boost branches only depends on both, its own parasitic resistances and effective duty cycle, and the parasitic resistances and effective duty cycle of the other phases [27]. This means in ideally, the current sharing between the two branches is automatically realized. Assuming that the duty cycles of the two boost branches are equal to d_1, it can be divided into two modes, i.e., $d_1 < 0.5$ and $d_1 > 0.5$, according to the range of d_1. The three-level converter on the HVS adopts the interleaved PWM voltage balance modulation proposed in [24]. Furthermore, the value and direction of the transfer power can be regulated by controlling the phase shift angle φ between v_{AB} and v_{CD}.

As shown in Fig. 2, there are 12 switching stages in a switching cycle. Considering the similarity, only six switching stages in half-switching cycle under the mode of $d_1 < 0.5$ are described. Fig. 3 shows the detailed equivalent circuits of these stages.

1) *Stage I [t_0–t_1) [see Fig. 3(a)]:* S_1, S_3, S_6, and S_7 are ON state. v_{AB} and v_{CD} are clamped to zero. The energy stored in the resonant tank is pumped back into the low-voltage

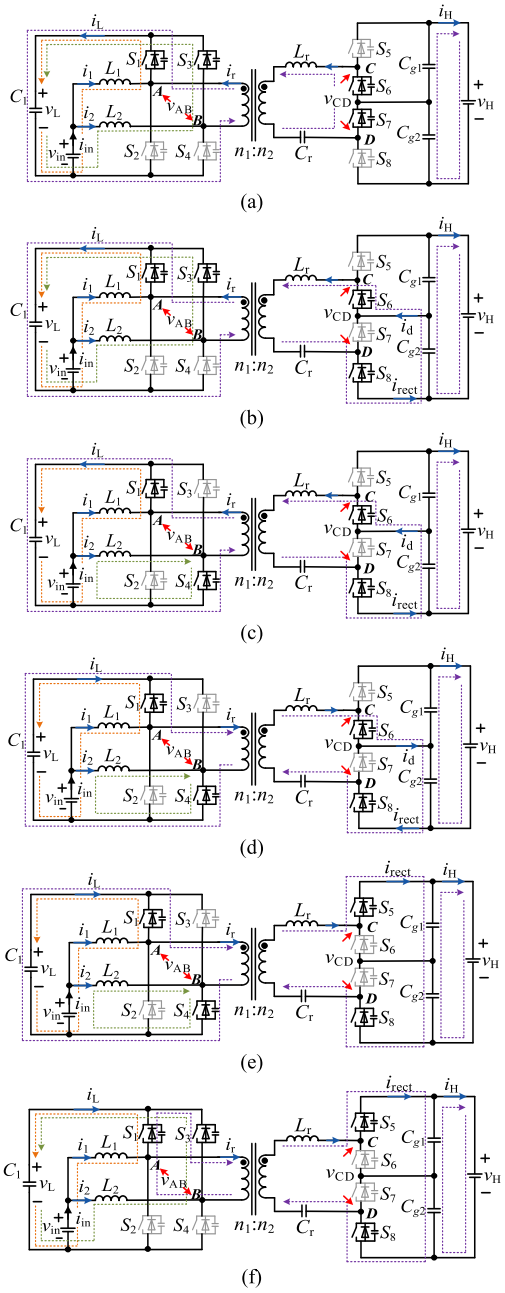

Fig. 3. Equivalent circuits of different stages in the forward mode. (a) [t_0-t_1). (b) [t_1-t_2). (c) [t_2-t_3). (d) [t_3-t_4). (e) [t_4-t_5), (f) [t_5-t_6).

bus through S_6 and S_7 and the body diodes of S_1 and S_4. The resonant current i_r decreases reversely. Meanwhile, C_1 is charged by v_{in} and L_1 and L_2 together through S_1 and S_3, the variation rate of input currents is expressed as

$$\frac{di_1}{dt} = \frac{di_2}{dt} = \frac{v_{in} - v_L}{L}. \tag{1}$$

2) *Stage II [t_1–t_2) [see Fig. 3(b)]:* At t_1, S_7 is turned OFF and S_8 is turned on, therefore $v_{CD} = v_H$. The resonant current i_r continues to decrease through S_6 and S_8 and the body diodes of S_1 and S_4.

3) *Stage III [t_2–t_3) [see Fig. 3(c)]:* At t_2, S_3 is turned OFF and S_4 is turned ON, therefore $v_{AB} = v_L$. i_r continues to decrease.

Meanwhile, since S_4 conducts, i_{L2} increases and its variation rate is expressed as

$$\frac{di_2}{dt} = \frac{v_{in}}{L}. \tag{2}$$

1) *Stage IV [t_3–t_4) [see Fig. 3(d)]:* At t_3, i_r decreases to zero and starts to increase positively. And the power is transferred from the LVS to the HVS through S_1, S_4, S_6, and S_8.
2) *Stage V [t_4–t_5) [see Fig. 3(e)]:* At t_4, S_6 is turned OFF and S_5 is turned ON. i_r commutates from S_6 to S_5, thus $v_{CD} = v_H$. Therefore, the HVS can generate a three-level equivalent AC power source with dc bias, where the dc bias is filtered out by the resonant capacitor C_r.
3) *Stage VI [t_5–t_6) [see Fig. 3(f)]:* At t_5, S_4 is turned OFF and S_3 is turned ON. v_{AB} is clamped to zero. i_r decreases gradually under the action of v_H. The power is transferred from the LVS to the HVS through S_3, the body diode of S_1 and S_5 and S_8. Meanwhile, L_2 is discharged again through S_2.

The operation principle of the converter under the mode of d_1>0.5 is similarly with that under the mode of $d_1 < 0.5$. The difference is that during the zero-level periods of v_{AB}, S_2 and S_4 are both ON state.

According to the above analysis, the LVS interleaved parallel current-fed structure can not only ensure that the continuity and low ripple characteristics of the input current, but also can control the LVS bus-voltage v_L by multiplexing the switches. The relationship between v_{in} and v_L is

$$v_L = \frac{v_{in}}{1 - d_1} \quad d_1 \in [0,\ 1). \tag{3}$$

Moreover, it can also control the internal phase shift angle D_1 of v_{AB}. The relationship between D_1 and d_1 is

$$\begin{cases} D_1 = 1 - 2d_1 & 0 \le d_1 < 0.5 \\ D_1 = 2d_1 - 1 & 0.5 \le d_1 < 1. \end{cases} \tag{4}$$

III. Power Characteristics and Optimized Modulation Strategy

A. Transfer Power Characteristics

The proposed resonant converter adopts the fixed-frequency control and the switching frequency is closed to the resonant frequency of the resonant tank. Therefore, the fundamental harmonics approximation method is used to analyze the steady-state operation characteristics. The fundamental equivalent circuit of the resonant converter is shown in Fig. 4, where v_{AB1}, v_{CD1} and i_{r1} are the fundamental components of v_{AB}, v_{CD} and i_r, respectively. All parameters are unified to the LVS, i.e.,

$$v_{CD1}{}' = \frac{n_1}{n_2} v_{CD1} \tag{5}$$

$$X_{Lr}{}' = \left(\frac{n_1}{n_2}\right)^2 X_{Lr},\ X_{Cr}{}' = \left(\frac{n_1}{n_2}\right)^2 X_{Cr}. \tag{6}$$

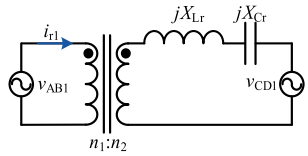

Fig. 4. Fundamental equivalent circuit of the resonant converter.

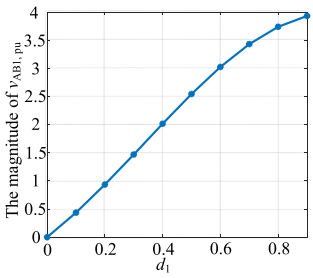

Fig. 5. Curve of magnitude of $v_{AB1,\mathrm{pu}}$ as a function of the duty-cycle.

The normalized impedance of the resonant tank is given

$$X_s = X_{Lr} + X_{cr} = \left(\frac{n_1}{n_2}\right)^2 \sqrt{\frac{L_r}{C_r}}(F - \frac{1}{F}) \tag{7}$$

where F is the normalized switching frequency and is defined as

$$F = f_s/f_r \tag{8}$$

where f_s is the switching frequency and f_r is the resonant frequency of the resonant tank

$$f_r = \frac{1}{2\pi\sqrt{L_r C_r}}. \tag{9}$$

For the purpose of convenience, all quantities are normalized with the base values. The base values represented by the subscript "B" are given as

$$V_B = v_{\mathrm{in}}, \quad I_{rB} = v_{\mathrm{in}}/X_s. \tag{10}$$

Combining (3) and (4), the normalized fundamental voltage of the two equivalent ac power sources are expressed as

$$v_{AB1,\,\mathrm{pu}}(t) = \frac{4}{\pi}\frac{\sin(d_1\pi)}{(1-d_1)}\sin(\omega_s t + \varphi\pi) \tag{11}$$

$$v_{CD1,\,\mathrm{pu}}(t) = \frac{4M}{\pi}\cos\left(D_2\frac{\pi}{2}\right)\sin(\omega_s t) \tag{12}$$

where the voltage gain M is defined as

$$M = \frac{n_1 v_{\mathrm{H}}}{2n_2 v_{\mathrm{in}}} \tag{13}$$

where $d_1 \in (0,\ 1]$, $D_2 \in [0,\ 1)$ and $\varphi \in [-0.5,\ 0.5]$.

The distribution curve of the magnitude of $v_{AB1,\,\mathrm{pu}}$ as a function of d_1 is drawn and shown in Fig. 5. When d_1 varies from 0 to 1, the magnitude of $v_{AB1,\,\mathrm{pu}}$ can be regulated from 0 to 4. It means the converter on the LVS realizes the buck-boost voltage conversion.

Using the principle of superposition, the normalized resonant current is solved and expressed as

$$i_{r1,\,\mathrm{pu}}(t) = \frac{4}{\pi}\left(\frac{\sin(d_1\pi)}{1-d_1}\sin(\omega_s t + \varphi\pi - \frac{\pi}{2}) - M\cos(D_2\frac{\pi}{2})\sin(\omega_s t - \frac{\pi}{2})\right). \tag{14}$$

By calculating the zero point of the first derivative of (14), the moment t_p, corresponding to the peak value of the resonant current fundamental component yields

$$\omega_s t_p = \arctan\left[\frac{\frac{\sin(d_1\pi)}{1-d_1}\sin(\varphi\pi)}{M\cos(D_2\frac{\pi}{2}) - \frac{\sin(d_1\pi)}{1-d_1}\cos(\varphi\pi)}\right]. \tag{15}$$

By substituting (15) into (14), the normalized magnitude and rms value of resonant current are solved and shown in (16) and (17) at the bottom of the page, respectively.

The normalized average transfer power in a switching cycle is derived as

$$P_{\mathrm{pu}} = \frac{1}{T_s}\int_0^{T_s} v_{CD1,\,\mathrm{pu}}(t) i_{r1,\,\mathrm{pu}}(t)dt = \frac{8M}{\pi^2}\frac{\sin(d_1\pi)}{(1-d_1)}\cos(D_2\frac{\pi}{2})\sin(\varphi\pi). \tag{18}$$

The transfer power coefficient G is defined as

$$G = \frac{\sin(d_1\pi)}{(1-d_1)}\cos(D_2\frac{\pi}{2})\sin(\varphi\pi). \tag{19}$$

From (19), the direction of the transfer power is determined by the external phase shift angle φ , while the average transfer power is determined by d_1, D_2 and φ together.

The four-dimensional curves of the transfer power and the rms value of resonant current as the functions of the three phase shifts are shown in the Figs. 6 and 7. For a certain transfer power, there are infinite combinations of the three degrees of freedom (d_1, D_2, φ) and the rms value of the resonant current varies in wide range under the different combinations. Therefore, it is necessary to properly introduce some constraints to obtain the exact relationship between the three degrees of freedom.

B. Optimal Modulation Strategy for Global Minimum RMS Value of Resonant Current

It is well known that under the same transfer power, the smaller the rms value of the resonant current is, the smaller the ON-state power loss of the power switches and the copper loss of the HFT and inductors will be. Therefore, in this article, the minimization of the rms value of the resonant current is introduced as an optimization objective into the modulation strategy. So that the efficiency of the converter can be increased.

In this section, the optimal operation point of (d_1, D_2, φ) is derived by minimizing the rms value of the resonant current under the desired transfer power. Therefore, the objective optimization function of rms value of the resonant current and the corresponding constraints is expressed as

$$\text{Minimize } i_{r1r,\,\mathrm{pu}}(d_1,\ D_2,\ \varphi) \tag{20}$$

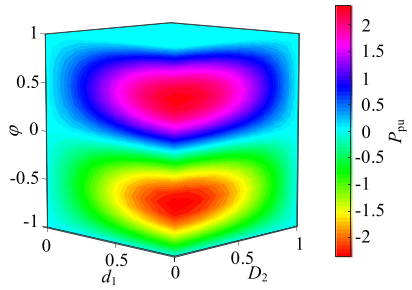

Fig. 6. Normalized average transfer power under different operation points.

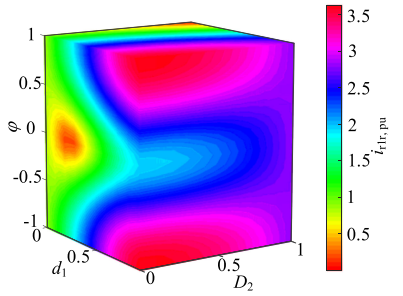

Fig. 7. Normalized RMS value of resonant current under different operation points.

subject to

$$\begin{cases} G(d_1,\ D_2,\ \varphi) - G^* = 0 \\ 0 \le d_1 < 1,\ \ 0 \le D_2 < 1,\ \ -0.5 \le \varphi \le 0.5 \end{cases} \tag{21}$$

where G^* is the index of the required transfer power.

The Lagrange multiplier method is used here to solve the above nonlinear optimization problem [28]. Combining (20) and (21), the relationship between d_1, D_2 and φ is expressed by the Lagrangian function L satisfying the Karush–Kuhn–Tucker (KKT) conditions as

$$\begin{aligned} L(d_1,\ D_2,\ \varphi,\ \lambda,\ \mu) &= i_{r1r,\,\mathrm{pu}}(d_1,\ D_2,\ \varphi) \\ &+ \lambda\left[G(d_1,\ D_2,\ \varphi) - G^*\right] + \sum_{j=1}^{q} \mu_j g_j(d_1,\ D_2,\ \varphi) \end{aligned} \tag{22}$$

where λ is the KKT multiplier for the equality constraint of the Lagrangian function L and the equality constraint is defined as (21), μ_j is the KKT multiplier for the inequality constraint of the Lagrangian function L and the inequality constraints are defined as

$$\begin{cases} g_1(d_1,\ D_2,\ \varphi) = -d_1 < 0 \\ g_2(d_1,\ D_2,\ \varphi) = d_1 - 1 < 0 \\ g_3(d_1,\ D_2,\ \varphi) = -D_2 \le 0 \\ g_4(d_1,\ D_2,\ \varphi) = D_2 - 1 < 0 \\ g_5(d_1,\ D_2,\ \varphi) = -\varphi - 0.5 \le 0 \\ g_5(d_1,\ D_2,\ \varphi) = \varphi - 0.5 \le 0. \end{cases} \tag{23}$$

Therefore, the objective operation point $G^* = (d_1{}^*,\ D_2{}^*,\ \varphi^*)$ of the objective function is solved by (22), which satisfies the KKT conditions as

$$\begin{cases} \left.\frac{\partial L}{\partial d_1}\right|_{G=G^*} = 0 \\ \left.\frac{\partial L}{\partial D_2}\right|_{G=G^*} = 0 \\ \left.\frac{\partial L}{\partial \varphi}\right|_{G=G^*} = 0 \\ \lambda \ne 0 \\ L(d_1,\ D_2,\ \varphi) - L(G^*) = 0 \\ \mu_j \ge 0 \\ g_j(G = G^*) \le 0 \\ \mu_j g_j(G = G^*) = 0 \ \ j = 1, \ldots, 6. \end{cases} \tag{24}$$

Substituting (17) and (18) into (20)–(24), the following equations are derived as

$$\begin{cases} D_2{}^* = 0 \\ M = \cos(\varphi\pi)\frac{\sin(d_1\pi)}{1-d_1} \\ G^* = M\tan(\varphi\pi). \end{cases} \tag{25}$$

The KKT candidate point is then solved, i.e., the global objective operation point of the minimum rms value of the resonant current $G^* = (d_1{}^*,\ D_2{}^*,\ \varphi^*)$ satisfies

$$\begin{cases} \frac{\sin(d_1{}^*\pi)}{1-d_1{}^*} = \sqrt{M^2 + G^{*2}} \\ D_2{}^* = 0 \\ \varphi^* = \frac{1}{\pi}\arctan(\frac{G^*}{M}) \end{cases} \tag{26}$$

where $0 < M < \sqrt{\pi^2 - G^{*2}}$.

Therefore, the operation principle of the proposed optimized modulation strategy is that, in order to ensure the effective voltage is applied for the longest time on the HVS, first fixing the internal phase shift angle D_2 of the HVS to 0, and then according to the desired transfer power, regulating φ, at the same time, to ensure the converter operates at the minimum rms value of the resonant current, d_1 is regulated to boost v_L to a suitable level. Combining with the optimized operation point shown in (26) and the parameters given in Table II, the curves of the control variables d_1 and φ as a function of the transfer power are drawn as Fig. 8. It can be seen from Fig. 8 that as the transfer power increases, both d_1 and φ increase monotonically under the proposed modulation strategy.

$$i_{r1\mathrm{P},\,\mathrm{pu}} = \frac{4}{\pi}\sqrt{\left(\frac{\sin(d_1\pi)}{1-d_1}\right)^2 - 2M\frac{\sin(d_1\pi)}{1-d_1}\cos(D_2\frac{\pi}{2})\cos(\varphi\pi) + \left(M\cos\left(D_2\frac{\pi}{2}\right)\right)^2} \tag{16}$$

$$i_{r1r,\,\mathrm{pu}} = \frac{\sqrt{8}}{\pi}\sqrt{\left(\frac{\sin(d_1\pi)}{1-d_1}\right)^2 - 2M\frac{\sin(d_1\pi)}{1-d_1}\cos\left(D_2\frac{\pi}{2}\right)\cos(\varphi\pi) + \left(M\cos\left(D_2\frac{\pi}{2}\right)\right)^2} \tag{17}$$

TABLE I
ZVS CONDITIONS OF VARIOUS SWITCHES

	ZVS Condition
S_1, S_3	$-\frac{G^*}{d_1}\left(\cos(d_1\pi)+\frac{M}{\pi}\right)<\frac{\pi X_S T_s}{8L_1}$
S_2, S_4	$\frac{G^*}{d_1}\left(\cos(d_1\pi)+\frac{M}{\pi}\right)<\frac{\pi X_S T_s}{8L_1}$

TABLE II
EXPERIMENTAL PARAMETERS

Parameter	value
Input Voltage (v_{in})	48V, 60V
High Side Voltage (v_H)	200V, 250V
Switching Frequency (f_s)	50kHz
Turn Ratio of Transformer (n_1: n_2)	1:2
Resonant Inductance (L_r)	70uH
Resonant Capacitance (C_r)	157.7nF
Input Inductance (L_1 , L_2)	1000 uH
Impedance of the input inductor (R_{L1}, R_{L2})	400mΩ
Bus Capacitance (C_1)	2000 uF
Divided Capacitance (C_{g1} , C_{g2})	47 uF
Power switch (SiC JFETs)	UF3C065040K3S: 650V/50A/42mΩ

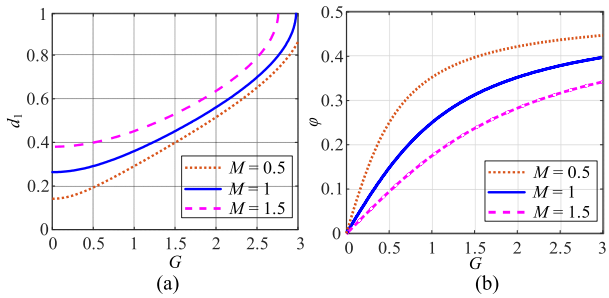

Fig. 8. Relation curves of control variables as a function of transfer power. (a) d_1 as a function of G. (b) φ as a function of G.

C. Time-Domain Verification of Optimized Modulation Strategy

Considering that the resonant converter is essentially an ac–ac power conversion system, the optimized modulation strategy can be easily verified in the time domain. Since the objective of the optimization modulation strategy is to minimize the RMS value of the resonant current, the phase between the resonant current and v_{CD1} should be evaluated. It is because for an ideal ac system, only when the converter operates at the unity power factor, the resonant current contains only the active power component and as a result, the rms value of the resonant current is the smallest.

Combining the optimal operation point obtained in the previous section, and substituting (25) and (26) into (11) and (12), the phase relationship of the amplitude of the equivalent voltage phasors $\vec{V}_{AB1,\,\mathrm{pu}}$ and $\vec{V}_{CD1,\,\mathrm{pu}}$ is derived as

$$V_{AB1\mathrm{m}}{}^{*}\cos(\varphi\pi)=V_{CD1\mathrm{m}}{}^{*}. \tag{27}$$

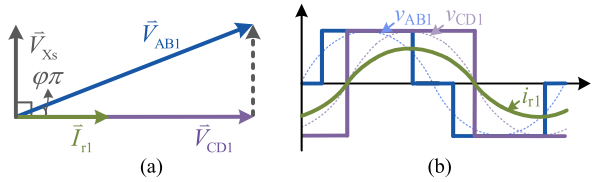

Fig. 9. Phasor diagram and operation waveforms under the optimized modulation strategy. (a) Phasor diagram. (b) Operation waveforms.

The phasor diagram of the fundamental equivalent converter and the operation waveforms of v_{AB}, v_{CD}, and i_r under the optimized modulation strategy are shown in Fig. 9. From Fig. 9, i_r is always in phase of v_{CD} and it ensures the converter operates at the minimum rms value of the resonant current in the entire power range. It can further improve the performance of the converter.

D. Soft-Switching Conditions Analysis

The soft-switching conditions of all power switches are analyzed in this section. The soft switching of the proposed converter is achieved with the help of the parasitic capacitor of the switch. The basic principle of soft switching is that the turn-OFF of the main conducting device diverts the current to the corresponding parasitic capacitors to charge one and discharge the other, resulting in a zero voltage (ZV) OFF. The ZV ON is achieved by gating on the in-coming device while the antiparallel diode is conducting. It means ZV OFF is realized naturally in the entire operation range, while ZV ON requires the constraints. Moreover, since i_{r1} is always in phase of v_{cd} under the proposed modulation strategy, the ZC on is always achieved for all the switches on the HVS. The ZV-ON constraint conditions for the primary-side switches are mainly discussed below.

The currents flowing through the power switches on the LVS is related to the dc input inductor currents and resonant current. Considering that the dc inductor currents for $d_1 < 0.5$ and $d_1 > 0.5$ are different, the soft-switching conditions in these two cases need to be calculated separately. The soft-switching conditions for the upper and lower power switches are expressed as

$$\begin{cases} i_r(2T_h-\frac{1-2d_1}{2}T_h) < i_1(2T_h-\frac{1-2d_1}{2}T_h) & d_1<0.5 \\ i_r(\frac{2d_1-1}{2}T_h) < i_1(\frac{2d_1-1}{2}T_h) & d_1>0.5 \end{cases} \tag{28}$$

$$\begin{cases} i_r(T_h+\frac{1-2d_1}{2}T_h) > i_1(T_h+\frac{1-2d_1}{2}T_h) & d_1<0.5 \\ i_r(T_h-\frac{2d_1-1}{2}T_h) > i_1(T_h-\frac{2d_1-1}{2}T_h) & d_1>0.5. \end{cases} \tag{29}$$

Combining with (14), (18) and the waveforms shown in Fig. 2, the above two equations are further expressed as

$$\begin{aligned} &-\frac{4v_{\mathrm{in}}}{\pi X_S}\left(\frac{\sin(d_1\pi)}{1-d_1}\sin(d_1\pi+\varphi\pi)-M\sin(d_1\pi)\right) \\ &<\frac{P_{\mathrm{out}}}{2v_{\mathrm{in}}}+\frac{v_{\mathrm{in}}d_1T_s}{2L_1} \\ &\frac{4v_{\mathrm{in}}}{\pi X_S}\left(\frac{\sin(d_1\pi)}{1-d_1}\sin(d_1\pi-\varphi\pi)-M\sin(d_1\pi)\right) \end{aligned} \tag{30}$$

$$> \frac{P_{\rm out}}{2v_{\rm in}} - \frac{v_{\rm in}d_1T_s}{2L_1}. \tag{31}$$

Substituting (26) into (30) and (31), (30) and (31) are simplified as

$$-\frac{G^*}{d_1}\left(\cos(d_1\pi)+\frac{M}{\pi}\right) < \frac{\pi X_S T_s}{8L_1} \tag{32}$$

$$\frac{G^*}{d_1}\left(\cos(d_1\pi)+\frac{M}{\pi}\right) < \frac{\pi X_S T_{\rm s}}{8L_1}. \tag{33}$$

The soft-switching conditions for primary-side switches of the proposed resonant converter are given in Table I. It can be seen (32) is always satisfied. Hence, the ZV ON of S_1 and S_3 is always achieved in the entire power range. While (33) is not always satisfied and difficult to find an exact range. Thus, the ZV ON of S_2 and S_4 is restricted. It can be seen from (33) the larger impedance of the resonant tank, the larger switching period, the smaller input inductor and the smaller voltage gain is conductive to expand the ZV-ON range of S_2 and S_4.

According to the above analysis, only the ZV ON of the lower switches S_2 and S_4 ON the LVS is restricted. The other switches all achieve ZVS. The reasonable design of topology parameters is conductive to expand the ZV-ON range of S_2 and S_4.

E. Power Loss Model and Comparison

In order to further quantitatively analyze the efficiency of the proposed optimization modulation strategy, the general power loss model of the proposed converter is established in this section. Furthermore, the power loss of the proposed modulation strategy and the fixed-frequency PWM strategy in the current-fed converter are compared in detail with each other based on the general power loss model.

The power loss of the converter mainly includes the switching loss $P_{\rm sw}$ and the conduction loss $P_{\rm cond}$ of the power switches, the copper loss $P_{\rm cop}$ and iron core loss $P_{\rm core}$ of the inductors and the transformer. According to the above analysis, only the ZV ON of the lower switches S_2 and S_4 on the LVS is limited. The other switches all achieve soft switching in the entire power range. In order to simplify the analysis, $P_{\rm sw}$ is neglected. Since the iron core loss is mainly related to the magnetic materials and the operation voltages and it is usually independent of the modulation strategy, $P_{\rm core}$ is also not discussed in this article. In addition, the fixed loss in the system such as the auxiliary power loss, the cooling loss and the fixed loss of the drive circuit is not discussed in the loss model.

1) *Conduction Loss*: the conduction loss is calculated as

$$P_{\rm cond} = {i_{\rm S,RMS}}^2 \cdot R_{\rm S} \tag{34}$$

where the $i_{S,\rm rms}$ denotes the RMS current flowing through the power switch in a switching period. The R_S denotes the ON-state resistance of the power switches.

Supposing that S_1-S_4 ON the LVS are exactly the same and the effect of the current ripple on the power loss is neglected in this article, the equivalent RMS currents of one leg on the LVS is solved and expressed as

$$i_{\rm B1,RMS} = i_{\rm B2,RMS} = \sqrt{\frac{1}{T_{\rm s}}\int_0^{T_{\rm s}} (i_1 - i_{\rm r1})^2 dt}$$
$$= \sqrt{{i_{\rm r1,RMS}}^2 + \left(\frac{P_{\rm out}}{2v_{\rm in}}\right)^2}. \tag{35}$$

Under the proposed modulation strategy, the resonant current always flow through two power switches on the HVS at the same time. Therefore, the rms current of all power switches on the HVS is calculated by

$$i_{\rm C\_S5,RMS} = i_{\rm C\_S6,RMS} = i_{\rm C\_7,RMS} = i_{\rm C\_S8,RMS} = \frac{n_1 i_{\rm r1,RMS}}{\sqrt{2}n_2}. \tag{36}$$

The total conduction loss of the power switches is calculated as

$$P_{\rm cond,Loss} = P_{\rm cond,LVS\_Loss} + P_{\rm cond,HVS\_Loss}$$
$$= 2\left({i_{\rm r1,RMS}}^2 + \left(\frac{P_{\rm out}}{2v_{\rm in}}\right)^2\right) R_{\rm S\_LVS}$$
$$+ 4\left(\frac{n_1 i_{\rm r1,RMS}}{\sqrt{2}n_2}\right)^2 R_{\rm S\_HVS}. \tag{37}$$

where $R_{S\_\rm LVS}$ denotes the ON-state resistance of the power switches on the LVS. $R_{S\_\rm HVS}$ denotes the ON-state resistance of the power switches on the HVS.

1) *Copper Loss*: The copper loss in the transformer coils and inductor coils are mainly related to the coil resistance $R_{tr\_\rm LVS}$, $R_{\rm tr\_HVS}$ and R_{L1}, R_{L2} and the rms current flowing through them, and is calculated by

$$P_{\rm cop,loss} = P_{\rm cop,L\_loss} + P_{\rm cop,Tr\_loss} \tag{38}$$

$$P_{\rm cop,L\_loss} = {i_1}^2 R_{\rm L1} + {i_2}^2 R_{\rm L2} \tag{39}$$

$$P_{\rm cop,Tr\_loss} = {i_{\rm r1,RMS}}^2 R_{\rm tr\_LVS} + \left(\frac{n_1 i_{r1,\rm RMS}}{n_2}\right)^2 R_{\rm tr\_HVS}. \tag{40}$$

It can be seen from the above analysis that the power loss is closely related to the rms value of the resonant current. Hence, reducing the RMS value of the resonant current effectively reduces power loss and improve the converter efficiency.

In order to evaluate the performance of the proposed modulation strategy, the RMS values of the resonant current and power loss of the proposed modulation strategy are compared with those of the fixed-frequency PWM strategy in [23]. The parameters used to compute the curves in this article are given in Table II. The SiC JFETs with part number UF3C065040K3S is used on both the LVS and the HVS in our experimental platform, hence the impedance of the switches ON the LVS and the HVS $R_{S\_\rm LVS}$ and $R_{S\_\rm HVS}$ are both 42 mΩ. By substituting the expressions of the RMS value of the resonant current of the proposed modulation strategy into the general power loss expression mentioned above, the exact power loss as a function of the desired transfer power under the proposed modulation strategy is obtained.

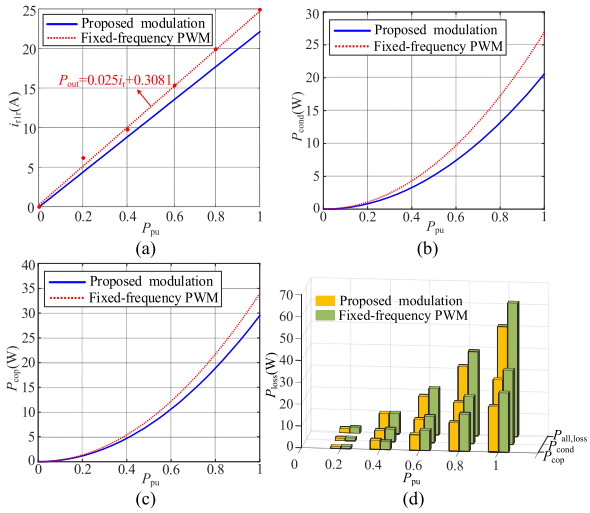

Fig. 10. Curves of various variables of the converter as a function of transfer power under different modulation strategies. (a) Resonant current amplitude. (b) Conduction loss. (c) Copper loss. (d) Total power loss.

Under the fixed-frequency PWM strategy, only d_1 is used as the control variable to regulate the transfer power. In [23], only the RMS value of the resonant current at various operating states of the converter is given. The exact analytic relationship between the RMS value of the resonant current and the desired transfer power is not shown. Therefore, in this section, the RMS values of the resonant current at different power are obtained through the simulation and the RMS value of the resonant current as a function of the desired transfer power is obtained by linear fitting, then the exact power loss under the fixed-frequency PWM strategy can also be obtained for comparison.

The distribution curves of the RMS values of the resonant current as a function of the transfer power under the two modulation strategies are drawn and shown in Fig. 10(a). The distribution curves of the conduction loss and the copper loss as a function of the transfer power are also drawn and shown in Fig. 10(b) and (c), respectively. The curves of the total power loss are shown in Fig. 10(d). From the analysis above and Fig. 10, compared with the fixed-frequency PWM strategy, the proposed modulation strategy effectively reduces the amplitude and RMS value of the resonant current and power loss. As the transfer power increases, the advantages of the proposed modulation strategy become more obvious.

IV. Experimental Verification

To verify the performance of the proposed converter and the optimized modulation strategy, a DSP + FPGA-based experimental prototype is built, as shown in Fig. 11. The experimental prototype is built by the modular approach. We have built some general half-bridge module with the SiC JFETs power switches. Combining with the schematic of the proposed converter shown in Fig. 1, we use four modules to make up the proposed converter in this experiment. The corresponding experimental parameters are given in Table II. Two dc voltage sources are used as the input sources of the dc ports on both sides, and two resistors are

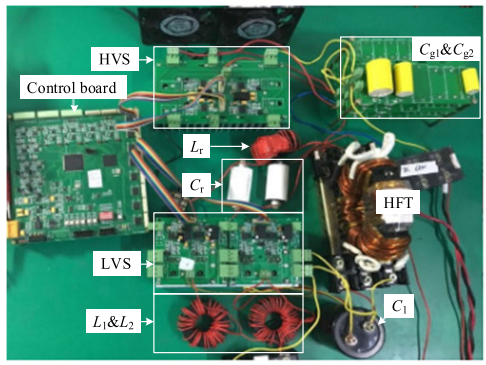

Fig. 11. Photograph of experimental platform based on DSP+FPGA.

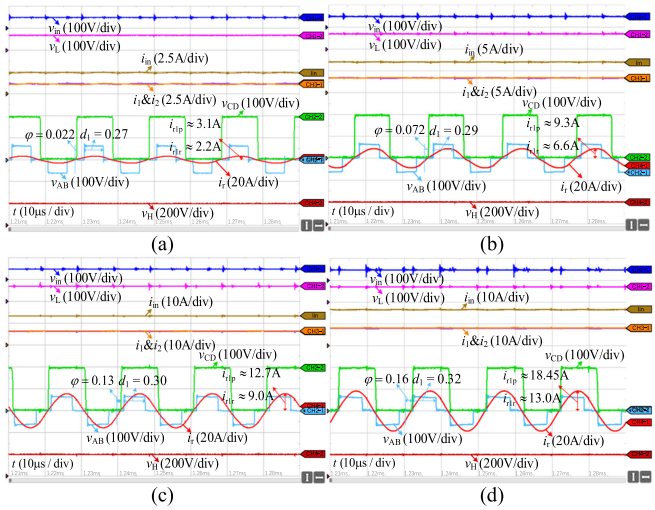

Fig. 12. Experimental results of optimized modulation in forward mode with $v_{\rm in}$ = 48 V and $v_{\rm H}$ = 200V. (a) $P_{\rm out}$ = 100W. (b) $P_{\rm out}$ = 300W. (c) $P_{\rm out}$ = 600W. (d) $P_{\rm out}$ = 800W.

connected in parallel to the two ports as the loads, respectively. In order to reduce the fluctuation of the output current of the dc power source, the larger inductance is selected to reduce the ripple of the inductor current. Further, the inductors, the switches and the drive circuits on the two branches are selected as the same as possible to ensure the average currents on the two branches are approximately the same as each other. A 100 W switching power supply is used as the auxiliary power to provide power for the driving circuit. All experiments are carried out under the open-loop conditions.

Fig. 12 shows the steady-state waveforms of the proposed converter in the forward mode under the optimized modulation strategy, with $v_{\rm in}$ = 48V and v_H = 200V. Fig. 12(a)–(d) shows the experimental results with the output power $P_{\rm out}$ = 100, 300, 600, and 800 W, respectively. The corresponding control variables d_1 and φ are determined by the minimum resonant current optimal conditions in (26). D_2 is always fixed at 0. φ and d_1 both increase with the increase of the transfer power. Correspondingly, v_L is regulated at the optimal value and $i_{\rm r1}$ is always in phase of $v_{\rm CD}$. Taking Fig. 12(b) as an example, when the transfer power is 300W, d_1 and φ calculated in combination with (26) are 0.278 and 0.066, respectively. The actual d_1 and φ read from the

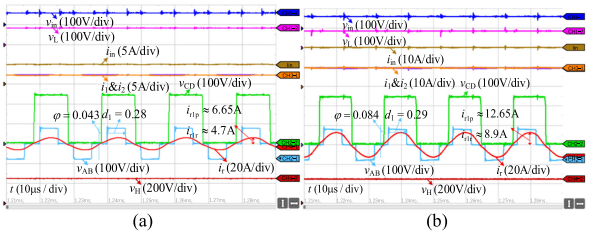

Fig. 13. Experimental results of optimized modulation in forward mode with $v_{\rm in} = 60$V and $v_{\rm H} = 250$V. (a) $\rm P_{out} = 280$W. (b) $\rm P_{out} = 600$W.

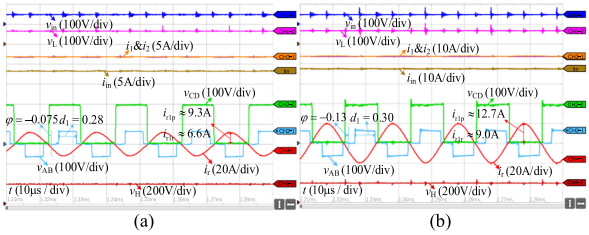

Fig. 14. Experimental results of optimized modulation in backward mode with $v_{\rm in} = 48$V and $v_{\rm H} = 200$V. (a) $P_{\rm out} = 300$W. (b) $P_{\rm out} = 600$W.

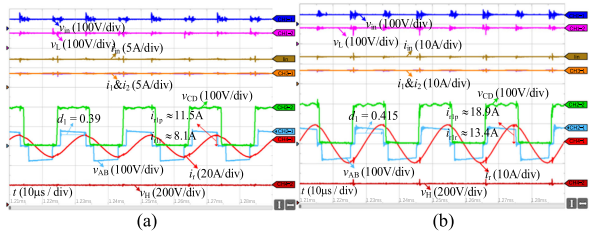

Fig. 15. Experimental results fixed-frequency PWM strategy in forward mode with $v_{\rm in} = 48$V and $v_{\rm H} = 200$V. (a) $P_{\rm out} = 300$W,.(b) $P_{\rm out} = 600$W.

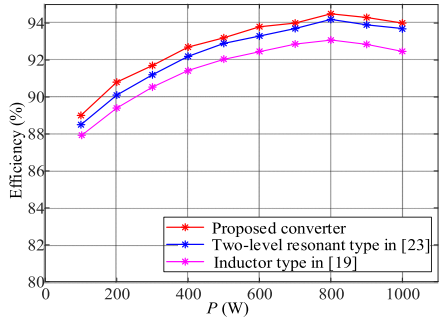

Fig. 16. Efficiency curves of three interleaved current-fed converters.

experimental waveforms are 0.29 and 0.072, respectively. The theoretical analysis and the experimental results are basically the same. Similarly, under various transfer power, the actual d_1 and φ read from the experimental waveforms are always close to those calculated from the theoretical expressions. The experimental results verified the theoretical analysis pretty well.

In order to evaluate the performance of the proposed converter and modulations strategy in a wider power and voltage conversion range, the input and voltages are varied and corresponding experimental results are tested. Fig. 13 illustrates the experimental waveforms of the optimized modulation strategy with $v_{\rm in} = 60$ V and $v_H = 250$ V. The experimental results show that under different port voltages, the proposed modulation strategy still ensures the converter operates with the minimum resonant current.

Fig. 14 shows the waveforms of the proposed converter and the modulation strategy in the backward mode with $v_{\rm in} = 48$ V and $v_H = 200$ V. Similar to the forward mode, when the converter operates at the optimal operation point calculated by (26) and the resonant current is always in phase of v_{CD}.

For the comparison, the performance of the proposed converter with the fixed-frequency PWM strategy is also tested experimentally. D_2 and φ are both fixed to 0, and the transfer power is regulated only by the duty cycle d_1. Fig. 15 (a) and (b) shows the experimental results with the same input/output voltages and transfer power as those of Fig. 12(b) and (c). From these figures, under the same transfer power, the RMS value and magnitude of the resonant current of the proposed strategy are always less than that of the fixed-frequency PWM strategy. Therefore, the advantages of the proposed strategy are verified once again in the experimental way.

In addition, the efficiency of the proposed converter under the proposed modulation strategy is tested with $v_{\rm in} = 48$V and $v_H = 200$V. The efficiency of the inductor-type converter in [19] and the two-level resonant-type converter in [23] is also tested based the built experimental platform and compared with that of the proposed one. The efficiency curves are all tested with the experimental parameters given in Table II. The tested efficiency curves are illustrated in Fig. 16. It can be seen that the efficiency of the proposed converter in the entire power range is always higher than those of other two converters. The maximum efficiency is about 94.5%.

Furthermore, in order to further verify the advantages of the resonant-type converter, it is compared with the inductor-type converter in term of the cost. Considering that the parameters of the magnetic components of the converters with the same rated voltage and rated power are generally the same, the cost of the magnetic components of the proposed converter and the other converters is considered to be the same. The rated parameters of the system used to calculate the cost are as follows. The input voltage is 48 V, the output voltage is 200 V and the rated transfer power is 1 kW. Since under the same transfer power, the input current and the voltage stress of the switches on the LVS of different topologies are the same, the transformer current on the primary side is compared emphatically.

To simplify the analysis, under the same transfer power, the RMS value of the transformer current of different topologies is regarded as the same. For the inductor-type topology, the peak value of the transformer current is at least twice of the average effective output current. The shape of the transformer current of the resonant-type one is close to the sinusoidal and the peak value of the transformer current is accordingly reduced to 1.414 of its rms value.

In the actual system application, the current rating of the switches is generally selected to be twice the maximum current flowing through the switches for the safety of the system. Hence,

TABLE III
DATA OF BIDIRECTIONAL DC–DC CONVERTERS

Parameter	Inductor	Resonant
RMS value of transformer current (A)	18	18
Peak value of transformer current (A)	36	25.5
Current rating of switch (A)	72	51
Ratio of current rating of switch	1	0.707

the current rating of the switches under different topologies are selected and given in Table III. Based on the current rating of the switch of the inductor-type topology, the ratio of the current rating of the resonant-type one is calculated and given in Table III.

From the above analysis, the current stress of the power switches in the resonant-type converter is only $1.414/2 = 0.707$ time of that of the inductor-type one. For sake of the comparison, it is regarded that the price of the power switch is proportional to the current rating. Hence, the cost ratio of the switches is qualitatively compared. The total cost of the power switches of the resonant-type one is 0.707 time of that of the inductor-type topology. The cost reduction ratio of the resonant-type topology is about 29.3% relative to the inductor-type topology. Although the comparison is not so precise, it still proves that the cost of the resonant-type converter is significantly reduced.

V. CONCLUSION

The proposed hybrid three-level current-fed series-resonant IBDC reduces the voltage stress of the power switches ON the HVS to half of the HVS bus voltage and provides one more control degree of freedom for improving the current characteristics of the equivalent resonant converter inside. The proposed modulation strategy ensures the converter operates with the minimum RMS value of the resonant current in the entire power range. Corresponding theoretical analysis and experiments have verified that the proposed converter and modulation strategy have higher efficiency and better voltage adaptability than the existing ones.

REFERENCES

[1] Z. Yin, L. Gong, C. Du, J. Liu, and Y. Zhong, "Integrated position and speed loops under sliding-mode control optimized by differential evolution algorithm for PMSM drives," *IEEE Trans. Power Electron.*, vol. 34, no. 9, pp. 8994–9005, Sep. 2019.

[2] J. L. Duarte, M. Hendrix, and M. G. Simoes, "Three-port bidirectional converter for hybrid fuel cell systems," *IEEE Trans. Power Electron.*, vol. 22, no. 2, pp. 480–487, Mar. 2007.

[3] B. Zhao, Q. Song, W. Liu, and Y. Sun, "Overview of dual-active-bridge isolated bidirectional dc–dc converter for high-frequency-link power-conversion system," *IEEE Trans. Power Electron.*, vol. 29, no. 8, pp. 4091–4106, Aug. 2014.

[4] F. Krismer, S. Round, and J. W. Kolar, "Performance optimization of a high current dual active bridge with a wide operation voltage range," in *Proc. 37th IEEE Power Electron. Specialists Conf.*, 2006, pp. 1–7.

[5] B. Zhao, Q. Song, W. Liu, and W. Sun, "Current-stress-optimized switching strategy of isolated bidirectional dc–dc converter with dual-phase-shift control," *IEEE Trans. Ind. Electron.*, vol. 60, no. 10, pp. 4458–4467, Oct. 2013.

[6] F. Wu, F. Feng, and H. B. Gooi, "Cooperative triple-phase-shift control for isolated dab dc–dc converter to improve current characteristics," *IEEE Trans. Ind. Electron.*, vol. 66, no. 9, pp. 7022–7031, Sep. 2019.

[7] X. Li and A. K. S. Bhat, "Analysis and design of high-frequency isolated dual-bridge series resonant dc/dc converter," *IEEE Trans. Power Electron.*, vol. 25, no. 4, pp. 850–862, Apr. 2010.

[8] Y. Shen, H. Wang, A. Al-Durra, Z. Qin, and F. Blaabjerg, "A bidirectional resonant dc–dc converter suitable for wide voltage gain range," *IEEE Trans. Power Electron.*, vol. 33, no. 4, pp. 2957–2975, Apr. 2018.

[9] J. Jung, H. Kim, M. Ryu, and J. Baek, "Design methodology of bidirectional CLLC resonant converter for high-frequency isolation of dc distribution systems," *IEEE Trans. Power Electron.*, vol. 28, no. 4, pp. 1741–1755, Apr. 2013.

[10] T. Jiang, J. Zhang, X. Wu, K. Sheng, and Y. Wang, "A bidirectional LLC resonant converter with automatic forward and backward mode transition," *IEEE Trans. Power Electron.*, vol. 30, no. 2, pp. 757–770, Feb. 2015.

[11] S. Luo and F. Wu, "Hybrid modulation strategy for IGBT-based isolated dual-active-bridge dc–dc converter," *IEEE J. Emerg. Sel. Topics Power Electron.*, vol. 6, no. 3, pp. 1336–1344, Sep. 2018.

[12] F. Z. Peng, H. Li, G.-J. Su, and J. S. Lawler, "A new ZVS bidirectional DC-DC converter for fuel cell and battery application," *IEEE Trans. Power Electron.*, vol. 19, no. 1, pp. 54–65, Jan. 2004.

[13] X. Pan, H. Li, Y. Liu, T. Zhao, C. Ju, and A. K. Rathore, "An overview and comprehensive comparative evaluation of current-fed-isolated- bidirectional dc/dc converter," *IEEE Trans. Power Electron.*, vol. 35, no. 3, pp. 2737–2763, Mar. 2020.

[14] F. J. Wu, S. Fan, X. Li, and S. Luo, "Bidirectional buck-boost current-fed isolated DC-DC converter and its modulation," *IEEE Trans. Power Electron.*, vol. 35, no. 5, pp. 5506–5516, May 2020.

[15] H. Xiao and S. Xie, "A ZVS bidirectional dc–dc converter with phase-shift plus PWM control scheme," *IEEE Trans. Power Electron.*, vol. 23, no. 2, pp. 813–823, Mar. 2008.

[16] Z. Ding, C. Yang, Z. Zhang, C. Wang, and S. Xie, "A novel soft-switching multiport bidirectional dc–dc converter for hybrid energy storage system," *IEEE Trans. Power Electron.*, vol. 29, no. 4, pp. 1595–1609, Apr. 2014.

[17] Y. Shi, R. Li, Y. Xue, and H. Li, "Optimized operation of current-fed dual active bridge dc–dc converter for PV applications," *IEEE Trans. Ind. Electron.*, vol. 62, no. 11, pp. 6986–6995, Nov. 2015.

[18] D. Sha, X. Wang, and D. Chen, "High-efficiency current-fed dual active bridge dc–dc converter with ZVS achievement throughout full range of load using optimized switching patterns," *IEEE Trans. Power Electron.*, vol. 33, no. 2, pp. 1347–1357, Feb. 2018.

[19] D. Sha, J. Zhang, X. Wang, and W. Yuan, "Dynamic response improvements of parallel-connected bidirectional dc–dc converters for electrical drive powered by low-voltage battery employing optimized feedforward control," *IEEE Trans. Power Electron.*, vol. 32, no. 10, pp. 7783–7794, Oct. 2017.

[20] Z. Guo, K. Sun, T. Wu, and C. Li, "An improved modulation scheme of current-fed bidirectional dc–dc converters for loss reduction," *IEEE Trans. Power Electron.*, vol. 33, no. 5, pp. 4441–4457, May 2018.

[21] J. Kan, S. Xie, Y. Tang, and Y. Wu, "Voltage-fed dual active bridge bidirectional dc/dc converter with an immittance network," *IEEE Trans. Power Electron.*, vol. 29, no. 7, pp. 3582–3590, Jul. 2014.

[22] G. Ortiz, J. Biela, D. Bortis, and J. W. Kolar, "1 Megawatt, 20 kHz, isolated, bidirectional 12kV to 1.2kV dc-dc converter for renewable energy applications," in *Proc. Int. Power Electron. Conf.*, 2010, pp. 3212–3219.

[23] H. Wu, K. Sun, Y. Li, and Y. Xing, "Fixed-frequency PWM-controlled bidirectional current-fed soft-switching series-resonant converter for energy storage applications," *IEEE Trans. Ind. Electron.*, vol. 64, no. 8, pp. 6190–6201, Aug. 2017.

[24] W. Liu, H. Jin, W. Yao, and Z. Lu, "An interleaved PWM method with better voltage-balancing ability for half-bridge three-level dc/dc converter," *IEEE Trans. Power Electron.*, vol. 33, no. 6, pp. 4594–4598, Jun. 2018.

[25] W. Li, S. Zong, F. Liu, H. Yang, X. He, and B. Wu, "Secondary-side phase-shift-controlled ZVS dc/dc converter with wide voltage gain for high input voltage applications," *IEEE Trans. Power Electron.*, vol. 28, no. 11, pp. 5128–5139, Nov. 2013.

[26] D. Liu, F. Deng, Q. Zhang, and Z. Chen, "Zero-voltage switching PWM strategy based capacitor current-balancing control for half-bridge three-level dc/dc converter," *IEEE Trans. Power Electron.*, vol. 33, no. 1, pp. 357–369, Jan. 2018.

[27] J. Gordillo and C. Aguilar, "A simple sensorless current sharing technique for multiphase dc–dc buck converters," *IEEE Trans. Power Electron.*, vol. 32, no. 5, pp. 3480–3489, May 2017.

[28] N. Rahbari-Asr and M. Chow, "Cooperative distributed demand management for community charging of PHEV/PEVs based on KKT conditions and consensus networks," *IEEE Trans. Ind. Informat.*, vol. 10, no. 3, pp. 1907–1916, Aug. 2014.